RESEARCH ARTICLE

WILEY **Asia-Pacific Journal of Chemical Engineering**   Curtin University

Effect of ionic radius on soot oxidation activity for ceria-based binary metal oxides

Anjana P. Anantharaman[1] | Hari Prasad Dasari[1] (iD) | Harshini Dasari[2] (iD) |
G. Uday Bhaskar Babu[3] (iD)

[1] Chemical Engineering Department, National Institute of Technology Karnataka, Mangalore, India

[2] Chemical Engineering Department, Manipal Institute of Technology, Manipal, India

[3] Chemical Engineering Department, National Institute of Technology Warangal, Warangal, India

Correspondence
Hari Prasad Dasari, Engineering Department, National Institute of Technology Karnataka, Mangalore 575025, India.
Email: energyhari@nitk.edu.in

Abstract

CeO_2 (C) along with binary metal oxides of $Ce_{0.9}M_{0.1}O_{2-\delta}$ (M = Sn, Hf, Zr, Gd, Sm, and La; CT, CH, CZ CG, CS, and CL) are synthesized using the EDTA–citrate method. Samples having an ionic radius smaller (CT, CH, and CZ) and larger (CG, CS, and CL) than Ce^{4+} are classified separately, and their soot oxidation activity is analyzed. The incorporation of dopant is confirmed from lattice constant variation in X-ray diffraction result. The critical descriptors for the activity are dopant nature (ionic radius and oxidation-state), single-phase solid solution, lattice strain, reactive (200) and (220) planes, Raman intensity ration (I_{ov}/I_{F2g}), optical bandgap, reducibility ratio, and surface oxygen vacancy. Smaller ionic radius, isovalent dopants (CH and CZ) create a defect site by lowering the optical bandgap along with improved surface oxygen vacancy concentration and thus enhanced soot oxidation activity. Aliovalent dopant with larger ionic radius shows the involvement of lattice oxygen in oxidation reaction by charge compensation mechanism. CL showed the highest activity amongst larger ionic radius samples.

KEYWORDS
ceria-based binary metal oxides, solid solution, ionic radius, optical band gap, oxygen vacancy

1 | INTRODUCTION

Thermodynamically stable redox sites of CeO_2 favours the cyclic change of $CeO_{2-\delta}$, which leads to the formation of oxygen vacancy. Defect structure of CeO_2 can be modified by the variation in temperature, oxygen partial pressure, and cation doping.[1] Addition of metal cation having different charge and ionic radius into ceria lattice improves the active oxygen mobility along with the creation of defective fluorite structure. Reddy et al.[2] studied the doping of CeO_2 with trivalent dopants of Sm, Eu, and Gd and concluded that oxygen defect created by Sm doping is significantly higher and the reduction temperature is lower, which results in higher soot oxidation activity for the Sm-doped sample.[2] A study by Rushton et al.[3] stated that with the dopant addition, oxygen transport is mediated by the oxygen vacancy that is created by the defect sites in the CeO_2 lattice.[3] Isovalent and aliovalent cation doping has lower oxygen vacancy formation energy in reactive facets of {111} and {110} and hence improves the vacancy formation due to structural deformation.[4,5] Addition of Zr has resulted in structural defect creation with different coordination number and thus improves the defect formation and distortion in oxygen sublattice.[4-6]

The rate of soot oxidation is generally predicted by the oxygen vacancy formation energy on the surface of metal oxides. Substitution of the cation with different

oxidation state to host lattice affects the oxygen vacancy formation energy with the formation of the hole at the top of the valence band. Isovalent dopant addition results in shortening the metal-oxygen bond in comparison with a Ce—O bond in CeO_2, which weakens the surface oxygen bond and lowers vacancy formation energy.[7] Presence of reduced ceria (Ce^{3+}) results in formation of active oxygen species that reacts with soot and forms CO/CO_2 and further results in oxygen vacancy. Oxygen vacancy created during this process can be further filled by gaseous oxygen or subsurface oxygen (accompanied by production of Ce^{4+}). The active oxygen eliminated from the surface reacts with soot and forms carbon oxides. Further, the cycle continues, and the entire soot gets oxidised.[8,9] Thus, the surface oxygen vacancy creation is critical for the soot oxidation reaction. Doping leads to defect sites with lower oxygen vacancy formation energy that enhance surface oxygen concentration, which takes part in soot oxidation reactions.[10] Descriptors are used to define the influence of different parameters on catalytic activity for soot oxidation reaction. A single parameter as a descriptor cannot be defined for doped metal oxide catalyst due to reaction complexity in the presence of dopants.[11] A combination that includes reducibility,[12] oxygen vacancy formation,[12] host structure,[13] phase cooperation,[14] and active sites[15] controls the soot oxidation activity and plays as one of the major descriptors. Host structural features depend upon the optical band gap,[16] dopant,[17] lattice parameter,[3] solid solution formation,[14] morphology,[13] and reactive facet planes.[5] It is critical to point out the specific descriptor that influences the soot oxidation activity of ceria-based catalysts because in most cases, it will be a combination of descriptors that will control the activity. Based on the previous study on single metal oxide having redox and nonredox properties, the catalytic activity varies for both the classes of metal oxides. For redox metal oxides, reduction temperature, ionic radius difference, and surface oxygen binding energy control the soot oxidation activity. On the other hand, for nonredox metal oxides, it is the ionic radius, lattice strain, and surface area that control the activity.[18] From the study, it is prominent that a common parameter of ionic radius affects the metal catalyst activity. Further, this study is undertaken to study the effect of ionic radius on soot oxidation activity for ceria-based binary metal oxides. Ceria-based binary metal oxides at the fixed composition of $Ce_{0.9}M_{0.1}O_{2-\delta}$ (M = Sn, Hf, Zr, Gd, Sm, and La) with smaller and larger ionic radius than host ion are discussed in this work. The binary metal oxides in this study are classified as higher ionic radius and smaller ionic radius samples. Ions with radius smaller than Ce^{4+} (0.97 Å), such as Hf^{4+} (0.83 Å), Zr^{4+} (0.84 Å),

and Sn^{4+} (0.81 Å),[19] are categorised as smaller ionic radius dopants. Similarly, dopants with ionic radius higher than Ce^{4+} are categorised as higher ionic radius samples (Gd^{4+} (1.05 Å), Sm^{4+} (1.08 Å), and La^{3+} (1.16 Å)).[19]

2 | EXPERIMENTAL DETAILS

2.1 | Material synthesis and characterisation

CeO_2 (C) along with binary metal oxides of $Ce_{0.9}M_{0.1}O_{2-\delta}$ (M = Sn, Hf, Zr, Gd, Sm, and La) represented as CT, CH, CZ CG, CS, and CL were synthesised using the EDTA–citrate method. AR grade chemicals were used for the synthesis of metal oxides. An EDTA–citrate complexing method reported earlier[18,20] was used to synthesise all the binary metal oxides. A black precursor solid obtained after heating at 150°C/24 hr in the oven was further calcined at 350°C/12 hr and 600°C/5 hr in air to obtain the required oxides.

X-ray diffraction (XRD) patterns of the samples were recorded on an XPERT Pro diffractometer. Lattice constant and crystallite size are calculated using Bragg's law and the Debye–Scherrer equation, respectively, from the corresponding XRD peaks. Brunauer–Emmett–Teller (BET) surface area analyser and pore volume are analysed using the SMARTSORB-92/93 instrument. Raman spectroscopy analysis was undergone in Bruker: RFS 27 model using a diode laser source (785 nm). CARL ZEISS SIGMA instrument was used to study scanning electron microscopy (SEM) analysis of the binary metal oxides, and Joel/JEM 2100 is used to analyse transmission electron microscopy (TEM) of the samples. Cary 5000 ultraviolet (UV)–vis diffuse reflectance spectroscopy (UV-vis DRS) with an integration sphere diffuse reflectance attachment was used to obtain UV-Vis near infrared (UV-Vis NIR) absorption behaviour of the samples. Tauc's plot was adopted to study the direct band gap energy values.[21] X-ray photoemission spectroscopy (XPS) of the samples are studied using Omicron ESCA+, and C correction was undergone for all the XPS peaks. The peak deconvolution was done using CasaXPS software. Further instrumental details are provided in previously reported work.[18]

2.2 | Soot oxidation activity measurement

The synthesised binary metal oxides were utilised as catalysts for soot oxidation reaction using standard Printex-U (carbon black, produced from the combustion of natural gas by Orion Engineered Carbons, used as a model

compound for diesel soot). The catalyst and soot were made into tight contact for 30 min with a catalyst:soot ratio of 4:1.[4,9,18] Bound moisture content was removed by preheating the sample at around 200°C. The prepared soot and catalyst mixture was loaded in a TG/DTA 6300 thermogravimetric analyser instrument and operated in a temperature range of 200°C –600°C with a heating rate of 10°C/min. Air flow at 100 ml/min was maintained for preheating and normal reactions.[4,9,18] The repeatability and order of the reaction were checked for multiple reactions.

3 | RESULTS AND DISCUSSION

3.1 | XRD analysis

The synthesised binary metal oxides are initially characterised using XRD analysis for phase identification. Diffraction peaks obtained for metal oxide series are shown in Figure S1. All samples (C, CT, CH, CZ CG, CS, and CL) displayed peak analogous to the cubic fluorite structure of CeO_2.[22] Apart from the fluorite phase, CT sample shows the rutile type tetragonal phase of SnO_2 in traces that confirm the existence of hybrid phase in the sample.[18] With the presence of secondary phase, the activity may be hindered for CT sample because the active sites cannot be readily available for the reaction.[23] Lattice constant, crystallite size, lattice strain, and facet plane ratio are calculated from the corresponding diffraction peaks, and their values are given in Table S1.

Figure 1a displays the lattice constant and lattice strain variation with the change in dopant ionic radius for all the binary metal oxide samples. It is evident from the lattice constant values that smaller and larger ionic radius samples have lower and higher lattice constants, respectively, in comparison with the C sample.[24] The higher lattice constant observed for CL is due to the higher ionic radius of La^{3+}. According to Reddy et al.,[25] oxygen vacancy formation energy and reducibility depend upon the dopant ionic radius, and thus the catalytic activity varies with the variation in cation radius. Consequently, the catalytic descriptors for larger and smaller ionic radius dopant for soot oxidation activity may also differ. Figure 1a confirms that all the doped sample shows higher lattice strain than C. With the improved lattice strain in doped sample, oxygen diffusion enhances, oxygen migration eases with enhanced defect density, and thus the oxidation reaction occurs quickly.[3] Hence, in the present study, all doped ceria-based binary metal oxides may have better catalytic activity than C. The intensity ratio of the reactive facet
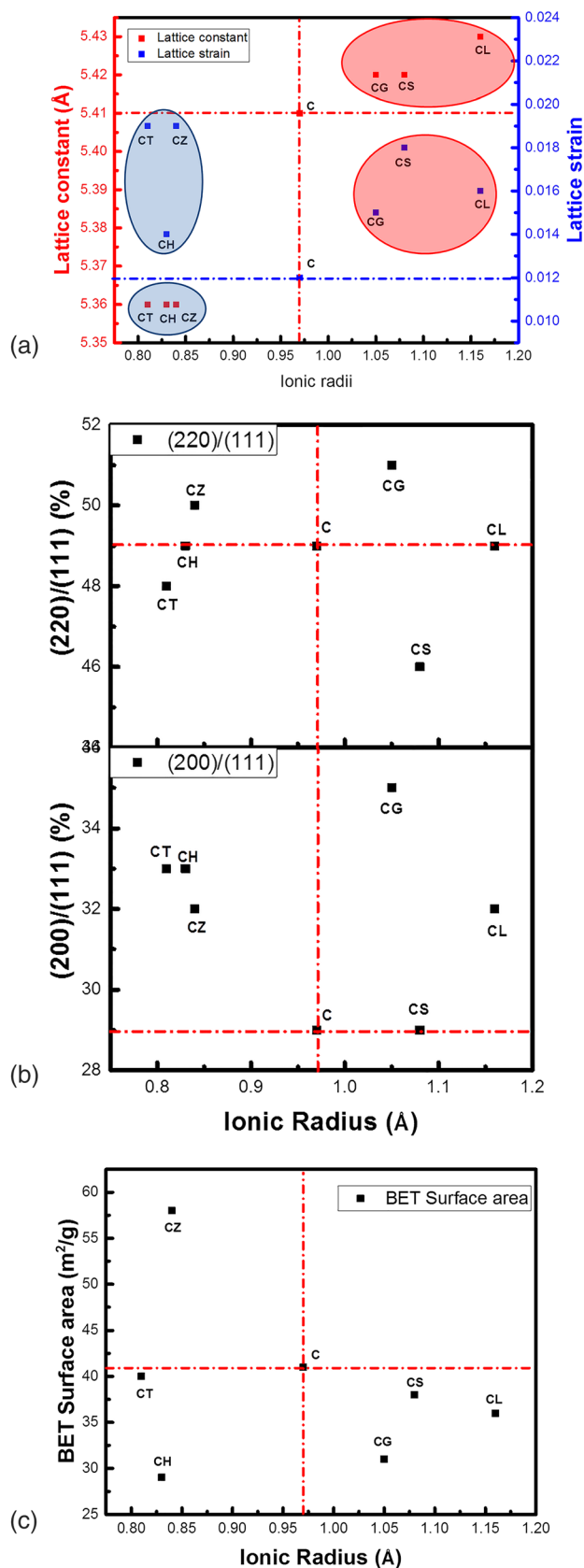
FIGURE 1 (a) Lattice constant and lattice strain variation, (b) (200)/(111) and (220)/(111) plane variation, and (c) . Brunauer–Emmett–Teller (BET) surface area variation of binary metal oxides with the increase in ionic radius

planes of (220)/(111) and (200)/(111) are calculated from the diffraction peaks and plotted with the change in dopant ionic radius and given in Figure 1b. Doped samples show almost the same or higher (200)/(111) ratio than pure C sample. On the other hand, for (220)/(111) planes, CH, CZ, CG, and CL have almost similar, or higher ratio than C. Aneggi et al.[26] reported a direct correlation between soot oxidation and exposed, less stable surface planes of (200) and (220) exist, due to higher specific activity of these planes in comparison with highly stable (111) plane. Shen et al.[27] stated that the reactive plane availability improves oxygen migration from the bulk and thus effectively enhances the catalytic activity. More than (220) planes, highly reactive (200) planes have the potential to improve the catalytic activity. As per the values of intensity of reactive planes and lattice strain, doped sample enhances catalytic activity compared with undoped C.

BET surface area and ionic radius variation are given in Figure 1c, which confirms that EDTA–citrate method results in a surface area value in the range of 25~45 m^2/g. However, CZ shows the highest surface area value out of all the samples. A direct relation between surface area and activity holds good for morphologically modified ceria samples studied by Aneggi et al.[26] Studies carried out by Piumetti et al.,[6] Thrimurthulu et al.,[28] and Guillén-Hurtado et al.[29] showed that the active sites that are in real contact with soot determines the catalytic activity instead of the surface area. Because the synthesis method adopted is the same for all the binary metal oxides, the variation in morphology may be limited. Particle size and degree of agglomeration of ceria-based binary metal oxides are also calculated and given in Table S1. Higher particle size than the crystallite size confirms the agglomeration of particles. Also, the degree of agglomeration value confirms that the sample gets agglomerated on the addition of dopant ions to pure ceria lattice.

Intrinsic structural descriptors that may affect the soot oxidation activity of ceria-based binary metal oxides as per XRD results are solid solution formation,[23] dopant ionic radius,[25] lattice strain,[3] and reactive (200) and (220) planes.[26] On the contrary, the surface area is not a descriptor in this study. Raman spectroscopy analysis is carried further to analyse the metal-oxygen bond and lattice defects in the binary oxide samples.

3.2 | Raman spectroscopy analysis

Raman spectra of the binary metal oxide series are given in Figure S2. The F_{2g} peak corresponding to the fluorite structure of ceria is evident in all the samples.[30]

Blueshift is observed in the F_{2g} peak for samples with smaller ionic radius and redshift for larger ionic radius samples.[31] Apart from the F_{2g} peak, oxygen vacancy is observed in all the samples with the presence of a shoulder peak at around 560~610 cm^{-1}.[32] The ratio of the intensity of oxygen vacancy to F_{2g} peak represented as (I_{OV}/I_{F2g}) confirms the availability of total oxygen within the lattice.[33] Figure 2 shows the variation of I_{OV}/I_{F2g} with the increase in ionic radius. Higher ratios are observed for CH and CL samples than C and lower for CT, CZ, CG, and CS samples. Aliovalent dopant addition leads to charge difference between dopant (Gd^{3+}, Sm^{3+}, and La^{3+}) and host cation (Ce^{4+}). The charge compensation mechanism results in the formation of oxygen vacancy with the dopant addition.[34] The Raman intensity ratio calculated using the data reflects the lattice oxygen from bulk.[35] With respect to change in oxygen vacancy concentration with the change in dopant ionic radius, a corresponding variation in vacancy formation mechanism may occur, which in turn affects the catalytic activity that will be discussed in further. Oxygen vacancy is the critical descriptor in controlling the catalytic activity due to their involvement in enhancing the oxidation reaction of soot.[36] However, the property that controls the mobility and creation of oxygen vacancy depends upon dopant nature and the vacancy formation mechanism. Further, the variation in sample morphology is studied using SEM and TEM analysis.

3.3 | SEM and TEM analysis

The SEM images of CT, CZ, and CL samples are displayed in Figure 3a, Figure 3b, and Figure 3c,
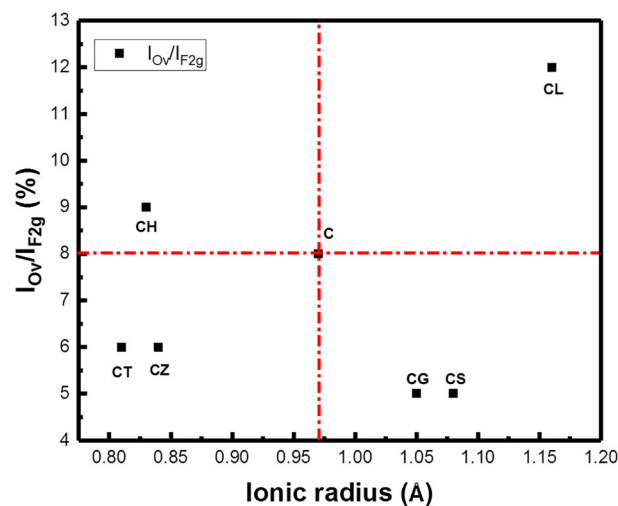
FIGURE 2 I_{OV}/I_{F2g} variation of binary metal oxides with the increase in ionic radius
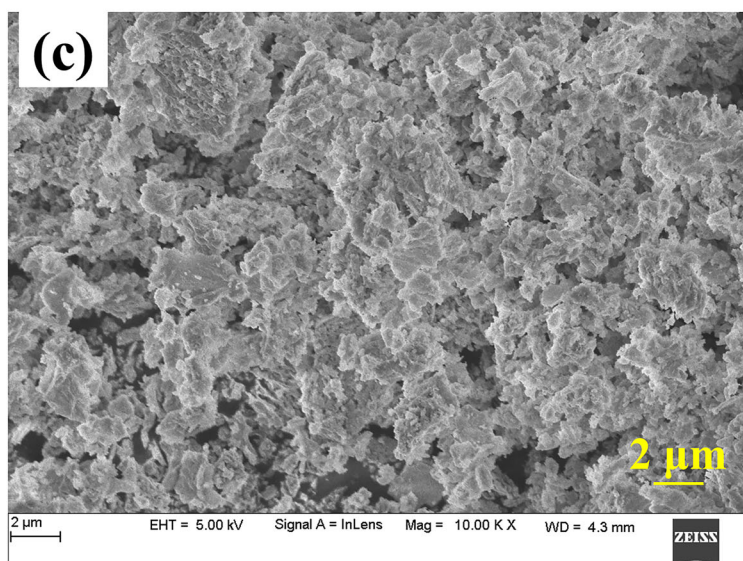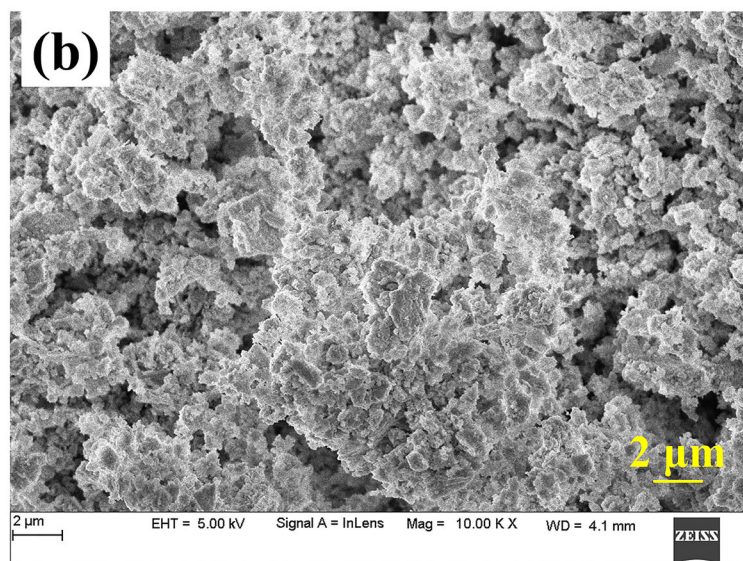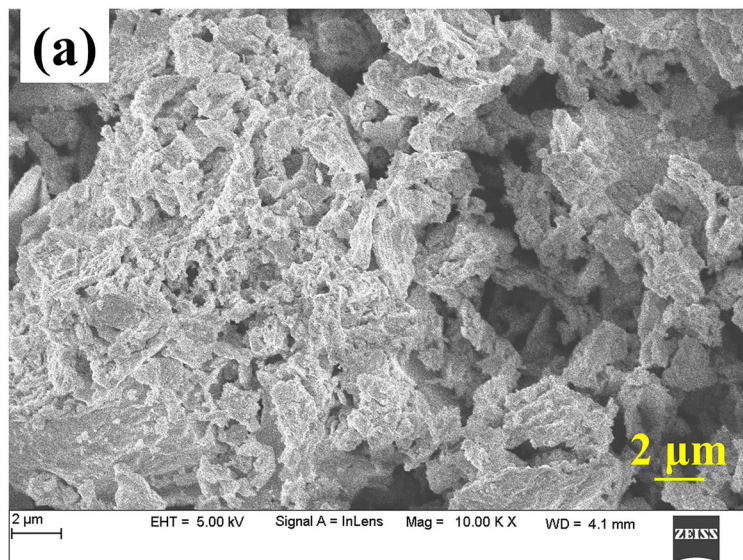
FIGURE 3 Scanning electron microscopy image of (a) CT, (b) CZ, and (c) CL binary metal oxides

respectively. Sample morphology confirms the agglomerated flaky nature without any specific shape. Not much deviation in morphology is evident from the SEM image of the samples. SEM image of remaining samples are provided in Figure S3. TEM micrographs of CZ and CL samples are given in Figure 4. TEM image in Figure 4a and Figure 4b for CZ and CL sample confirms similar morphology, and the nano-particles are agglomerated. Figure 4c and Figure 4d shows HR-TEM image of CZ and CL samples with the interplanar distance of lattice fringes, corresponding to intense (111) plane. Surface morphology significantly influences the soot oxidation activity due to structural modifications.[26,37] With the synthesis procedure for all binary metal oxides remaining the same, the structural morphology remains almost the same even with the dopant addition. The effect of morphology can be neglected along with BET surface area for soot oxidation activity. Further, the optical band gap effect is analysed using UV-vis DRS analysis.

3.4 | UV-vis DRS analysis

The absorbance spectra in UV and visible range of respective samples are obtained and given in Figure S4. Peaks corresponding to charge transaction and interband transaction matches well in all the samples.[1] The direct band gap is calculated from the absorbance peaks using Tauc's plot (see Figure S5).[21] Figure 5 shows the optical band gap of both smaller and larger ionic radius samples. Band gap value obtained matches with the literature values reported.[38] Obvious relation exists between the ionic radius and optical band gap for the samples. Smaller ionic radius samples with a lower lattice constant have lower band gap values, and on the other hand, larger ionic radius has higher band gap values. The decrease in band gap value results in easy formation of oxygen vacancy or defect sites which may enhance the catalytic activity.[16] The band gap variation is directly proportional to the lattice constant due to the change in metal interaction.[39]
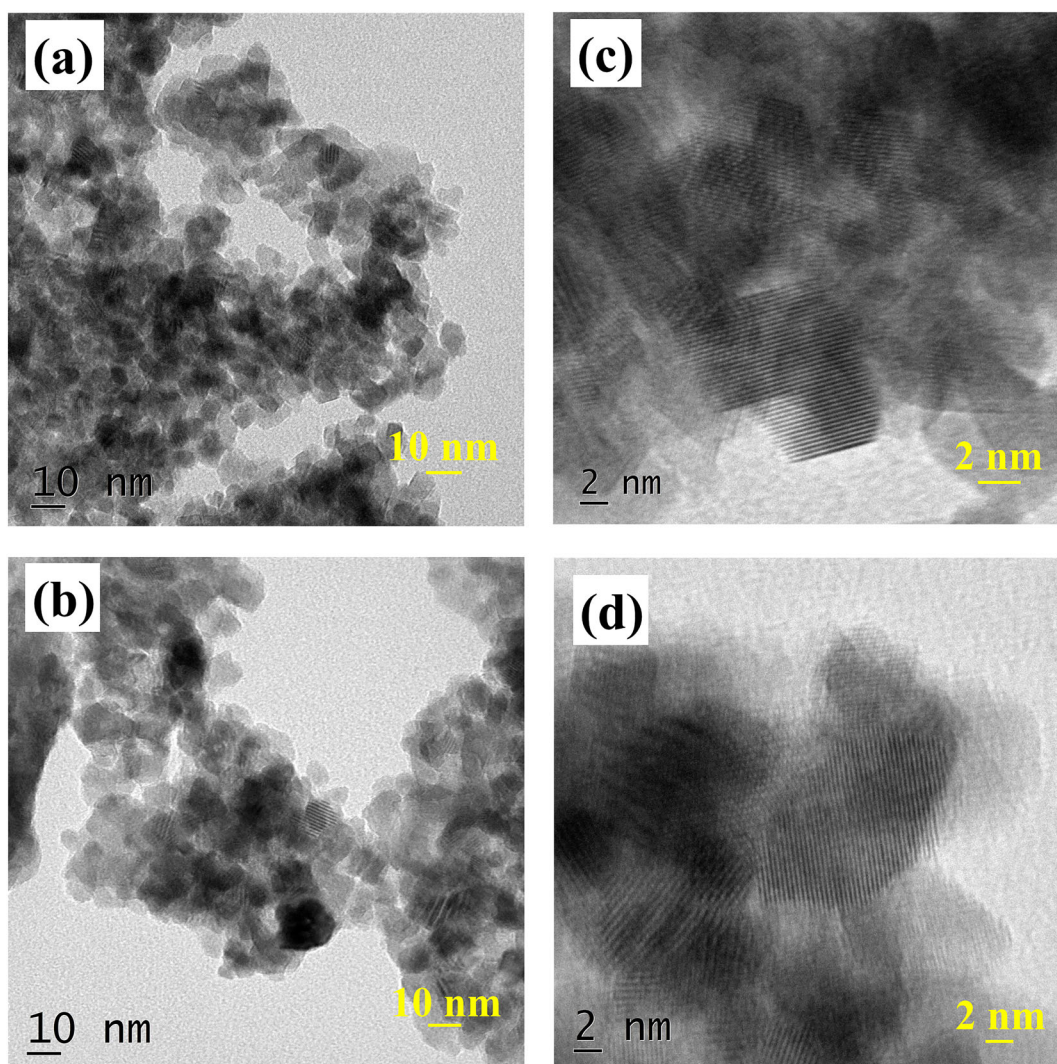
FIGURE 4 Transmission electron microscopy (TEM) image of (a) CZ and (b) CL sample and HR-TEM image of (c) CZ and (d) CL sample
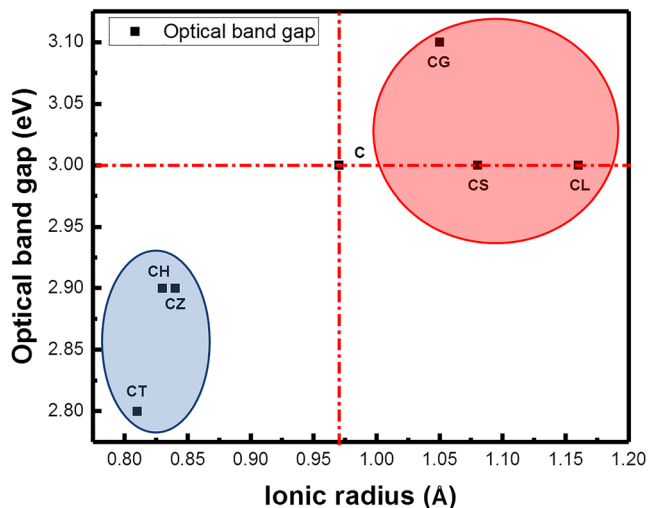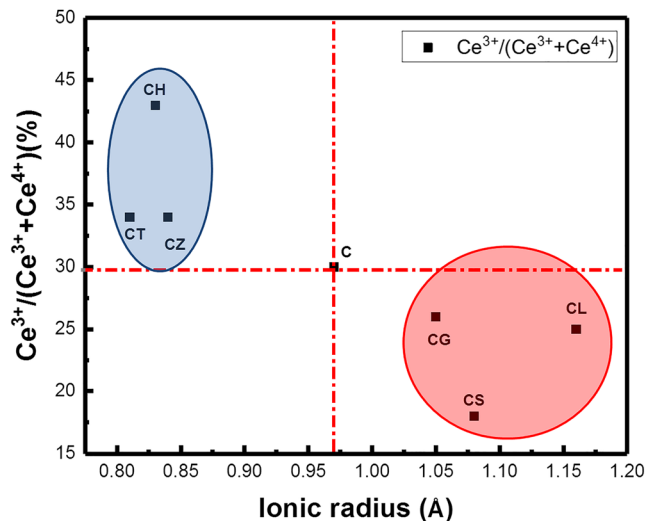
FIGURE 5 Optical band gap variation of binary metal oxides with the increase in ionic radius

FIGURE 6 $Ce^{3+}/(Ce^{3+}+Ce^{4+})$ variation of binary metal oxides with the increase in ionic radius

The decrease in band gap value corresponds to an increase in defect density[30] and Ce^{3+} concentration.[38] Mukherjee et al.[31] showed a lowering of the band gap with the dopant addition, due to the increase in oxygen defect density calculated from Raman analysis.[31] In this light, the optical band gap along with oxygen vacancy from Raman study may be a critical intrinsic descriptor that has potential influencing the soot oxidation activity apart from the structural descriptor. Based on the results obtained, the trend in I_{Ov}/I_{F2g} matches well with the obtained optical band gap specifically for smaller ionic radius samples. In contrary, for larger ionic radius binary metal oxides, CL with higher I_{Ov}/I_{F2g} ratio shows a higher optical band gap value. Thus, the oxygen vacancy calculated from Raman spectra can be related to the band gap value of the sample. The change in oxygen vacancy formation mechanism for isovalent and aliovalent might be the reason for the difference in optical band gap trend. Further, the Ce^{3+} concentration and surface oxygen concentration are calculated using XPS analysis.

3.5 | XPS analysis

The elemental oxidation state of the sample was analysed using XPS analysis of Ce 3d and O 1s are shown in Figure S6 and Figure S7, respectively. Spin-orbital multiplets of Ce $3d_{5/2}$ and Ce $3d_{7/2}$ contribute to multiple oxidation states of Ce^{3+} and Ce^{4}, respectively and are confirmed in all the samples.[28,40] Reducibility ratios are calculated based on the deconvoluted peaks as $(Ce^{3+}/(Ce^{3+}+Ce^{4+}))$ and are plotted for all the samples with the increase in ionic radius (see Figure 6).[41] From the figure, it is well evident that the reducibility ratio is higher

for smaller ionic radius samples rather than larger ionic radius samples. Samples having higher reducibility shows better catalytic activity due to improved redox cycle for soot oxidation reaction.[42] Lower reducibility ratio for larger ionic radius samples could be due to reduced redox cycle, which could be related to oxygen vacancy formation mechanism as discussed earlier and analysed further using O 1s XPS.[9] On deconvoluting the peaks for O 1s, three oxygen peaks are seen that corresponds to lattice oxygen (O_α), surface oxygen (O_β), and weakly bound oxygen (O_γ), respectively.[35,41] The relative ratio of surface oxygen to the total oxygen ($O_\beta/O_\alpha + O_\beta + O_\gamma$) plot with the increase in ionic radius shown in Figure 7 relates the surface oxygen mobility of the sample.[41] The surface oxygen vacancy concentration is higher for CH amongst
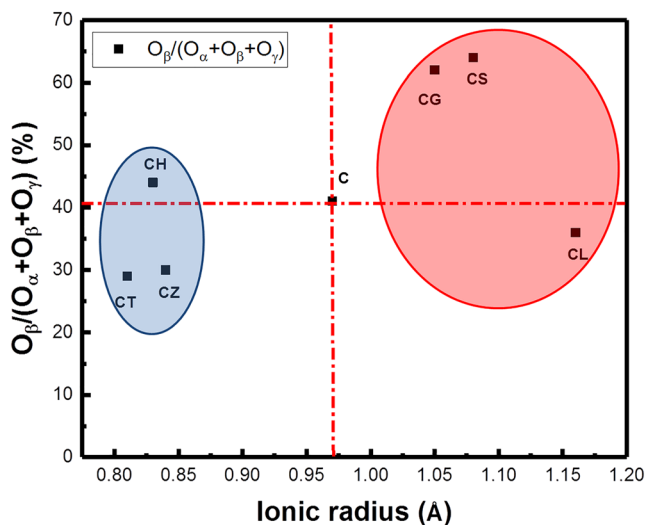
FIGURE 7 $O_\beta/(O_\alpha + O_\beta + O_\gamma)$ variation of binary metal oxides with the increase in ionic radius

smaller ionic radius samples and for CS and CG amongst larger ionic radius samples. With an increase in surface oxygen concentration, a relative increase in oxygen mobility can enhance the catalytic activity of the sample.[41] Despite better I_{ov}/I_{F2g} ratio from Raman results for aliovalent CL, surface oxygen vacancy calculated from XPS is low. Because the surface oxygen concentration varies with the change in dopant ionic radius, the oxygen vacancy formation mechanism also might be different in these samples. Apart from oxygen vacancy for CL, other factors can influence the oxidation reaction and may affect the catalytic activity. Thus, the critical descriptor defined for soot oxidation reaction is oxygen vacancy as per basic characterisation study. Lower lattice oxygen diffusion than surface oxygen corresponds to lowering the activity, thus it is essential to find the concentration of oxygen vacancy.[9] The catalytic activities for soot oxidation reaction are studied further, and the detailed analyses of different descriptors are discussed.

3.5.1 | Soot oxidation activity

The soot conversion profiles of all samples are provided in Figure S8 and Figure 8, which show the variation in T_{50} temperature with the ionic radius. It is evident that the T_{50} temperatures of doped samples are lower than C due to the improved lattice strain and (200) planes as studied from XRD. Amongst the smaller ionic radius samples (CT, CH, and CZ), CT has significantly lower activity ($T_{50} = 450°C$) due to secondary phase formation as evident from XRD peaks which hinders the active site contact as reported earlier.[18,43,44] Almost similar T_{50} temperature obtained for CH and CZ (430°C and 425°C,

respectively) could be due to the similar dopant ionic radius with the same oxidation state of 4+. Although smaller ionic radius dopants are added to ceria lattice, the lattice constant and lattice strain has been decreased and increased, respectively which confirms the incorporation of dopants into ceria lattice. Highly reactive (200) and (220) plane availability in higher quantity for CH and CZ, may result in reducing the energy for oxygen vacancy formation and results in lower T_{50} temperature. Even though CZ has a higher surface area, correspondingly T_{50} temperature variation is not evident, which indicates the surface area is not directly influencing soot oxidation activity of samples in this study. However, optical band gap value has reduced although doping C with smaller ionic radius dopants. As the band gap reduced, defect sites are formed, which eases oxygen vacancy formation that depends upon the vacancy formation mechanism and ionic radius. Isovalent Hf^{4+} and Zr^{4+} do not create defect sites by charge compensation. Instead, ionic radius difference between host and dopant ion improves the oxygen migration within the ceria lattice and enhances surface oxygen vacancy creation, thus aids the soot oxidation reaction. Doping smaller ionic radius sample has reduced the optical band gap, which is critical for defect site creation that could be a primary descriptor for catalytic activity.

The cations of 3+ oxidation state and larger ionic radius (CG, CS, and CL) are doped into host Ce^{4+} of different charge (aliovalent dopants). The samples display a higher T_{50} temperature than smaller ionic dopant as shown in Figure 8. CL shows the lowest T_{50} temperature of 450°C compared with CG and CS with a T_{50} temperature of 490°C and 480°C, respectively. The lattice constant is higher than C samples due to the higher ionic radius of the dopants. Highly reactive facet planes of (200) and (220) in CG and CL improves the oxidation reaction by lowering the oxygen vacancy formation energy. Oxygen concentration calculated is higher for CL compared with CG and CS due to the addition of highest ionic radius La^{3+} ion by charge compensation mechanism. The optical band gap is higher for CG and almost similar for CS and CL samples. Because oxygen vacancy formed due to charge compensation mechanism (lattice oxygen) has lower diffusion than surface oxygen as observed in smaller ionic radius, the catalytic activity is reduced for larger ionic radius samples in comparison with smaller ionic radius samples. Amongst these samples, larger ionic radius dopant (La^{3+}) creates higher lattice oxygen vacancy and shows improved catalytic activity. The dopant ionic radius (lattice constant), oxygen vacancy and optical band gap values are the significant descriptors for soot oxidation activity. Figure S9 depicts the trend in activity with the change in ionic
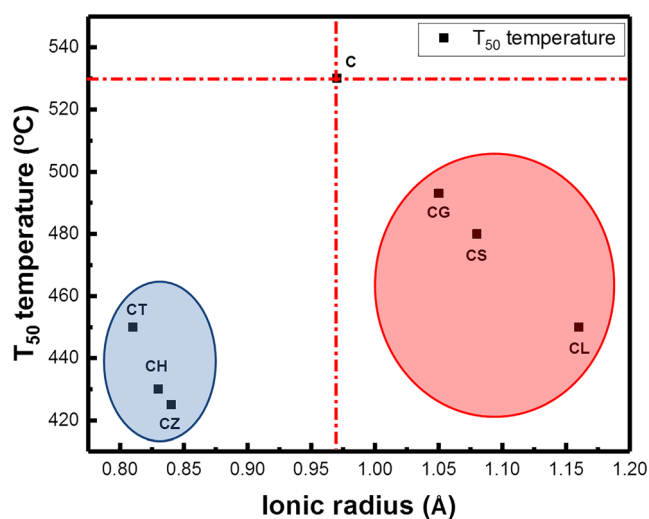
FIGURE 8 T_{50} temperature variation of binary metal oxides with the increase in ionic radius

radius, lattice constant, and optical band gap. Thus, the soot activity is highly dependent on the ionic properties of dopant added to the ceria lattice as per the study.

3.5.2 | Factors affecting the soot oxidation activity

CZ nanoparticles with 90:10 composition synthesised by hydrothermal method having the same composition as the current study has shown a T_{50} temperature of ~491°C,[6] which is considerably higher than the T_{50} temperature (~425°C) obtained in this study, might be because of very low surface area (~2 m²/g) reported, which is unfavourable for the catalytic activity. Even though catalytic activity does not directly correlate with surface area, a minimum value is necessary to ensure sufficient contact between soot and catalyst.[6] Despite having a very high surface area (84 m²/g) for CZ with 80:20 composition ratio synthesised by coprecipitation method studied by Mukherjee et al., lower activity (T_{50} = ~540°C) is justified due to low surface oxygen vacancy for the sample.[17] Similarly for CL and CH samples, T_{50} temperature of ~465°C and ~407°C, respectively, are obtained that are considerably lower than the value obtained in our study,[17] could be due to the difference in synthesis method, calcination conditions, and sample composition.

Oxidation of soot occurs by utilising the surface-adsorbed oxygen on the catalyst. However, the primary descriptors that have potential in influencing the catalytic activity are the nature of the dopant (isovalent or aliovalent), ease of solubility with host structure (solid solution or hybrid phase), dopant ionic radius (smaller or larger), and optical band gap value (lower or higher). However, all these descriptors are influencing the oxygen vacancy formation that is controlling the oxidation reaction of soot. Thus, the critical descriptor that needs to be improved is the surface oxygen vacancy concentration by varying different structural and intrinsic properties. Isovalent dopants of the smaller ionic radius can directly influence defect site formation that enhances the oxidation reaction by forming an intermediate level with lower energy, and thus the oxygen defect sites can be formed easily. Defect sites or active oxygen site further take part in oxidation reaction.[23] If the larger ionic radius dopant is aliovalent, charge difference exists between host ion and cation and further charge compensation mechanism leads to vacant oxygen sites that smoothly involve in oxidation reaction.[34] With the variation in dopant size and charge, the reaction mechanism varies, so does the T_{50} temperature also.

4 | CONCLUSIONS

Binary metal oxides of C, CT, CH, CZ CG, CS, and CL were synthesised using the EDTA–citrate method. The whole sample series are classified as smaller ionic radius dopants (CT, CH, and CZ) and larger ionic radius dopants (CG, CS, and CL) depending upon the ionic radius of the dopant added in comparison with Ce^{4+} ionic radius. Hybrid phase formation deteriorates the activity of CT (T_{50} = 450°C) sample. The descriptor that controls the catalytic activity primarily depends upon the nature of the dopant material (aliovalent and isovalent dopant). Thus, the primary descriptor for binary metal oxide series is ionic radius and dopant charge. Further with the addition of isovalent, smaller ionic radius dopants, defect site formation lowers the optical band gap with the potential in lowering oxygen vacancy formation energy and thus enhance the soot oxidation reaction. The T_{50} temperature obtained for isovalent CH and CZ are almost similar to 430°C and 425°C, which has almost the same optical band gap of around 2.9 eV with enhanced surface oxygen concentration. Soot oxidation activity of aliovalent dopants with larger ionic radius is dependent on oxygen vacancy formation mechanism by charge compensation. CL with higher oxygen vacancy has higher activity (T_{50} = 450°C) compared with other larger ionic radius dopants, CS (T_{50} = 490°C) and CG (T_{50} = 480°C). Due to lower lattice oxygen diffusion compared with surface oxygen, larger ionic radius sample shows lower activity than smaller ionic radius samples. Overall, soot oxidation activity for all binary metal oxide is controlled by optical band gap.

AUTHOR CONTRIBUTIONS

A. P. A. obtained all the experimental data. U. B. B. and H. D. provided XRD and BET surface area data, respectively. H. P. D. conceived the study. A. P. A. and H. P. D. analysed all the experimental data, and all authors contributed to writing and editing the document.

ORCID

Hari Prasad Dasari 🔴 https://orcid.org/0000-0003-2921-8102

Harshini Dasari 🔴 https://orcid.org/0000-0001-9410-4369

G. Uday Bhaskar Babu 🔴 https://orcid.org/0000-0002-1208-5238

REFERENCES

1. Calvache-Muñoz J, Prado FA, Rodríguez-Páez JE. Cerium oxide nanoparticles: synthesis, characterization and tentative mechanism of particle formation. *Colloids Surf A Physicochem Eng Asp*. 2017;529(May):146-159.

2. Reddy BM, Vinodkumar T, Durgasr Naga D, Rangaswamy A. Synthesis and characterization of nanostructured $Ce_{0.8}M_{0.2}O_{2-\delta}$ (M = Sm, Eu, and Gd) solid solutions for catalytic CO oxidation. *Proc Natl Acad Sci India Sect A Phys Sci*. 2016;87(1):155-161.

3. Rushton MJD, Chroneos A, Skinner SJ, Kilner JA, Grimes RW. Effect of strain on the oxygen diffusion in yttria and gadolinia co-doped ceria. *Solid State Ion*. 2013;230:37-42.

4. Vinodkumar T, Rao BG, Reddy BM. Influence of isovalent and aliovalent dopants on the reactivity of cerium oxide for catalytic applications. *Catal Today*. 2015;253:57-64.

5. Aneggi E, de Leitenburg C, Llorca J, Trovarelli A. Higher activity of diesel soot oxidation over polycrystalline ceria and ceria–zirconia solid solutions from more reactive surface planes. *Catal Today*. 2012;197(1):119-126.

6. Piumetti M, Bensaid S, Russo N, Fino D. Investigations into nanostructured ceria-zirconia catalysts for soot combustion. *Appl Catal Environ*. 2016;180:271-282.

7. Hu Z, Metiu H. Effect of dopants on the energy of oxygen-vacancy formation at the surface of ceria: local or global? *J Phys Chem C*. 2011;115(36):17898-17909.

8. Liu S, Wu X, Tang J, et al. An exploration of soot oxidation over CeO_2-ZrO_2 nanocubes: do more surface oxygen vacancies benefit the reaction? *Catal Today*. 2017;281:454-459.

9. Krishna K, Bueno-López A, Makkee M, Moulijn JA. Potential rare earth modified CeO_2 catalysts for soot oxidation. *Appl Catal Environ*. 2007;75(3-4):189-200.

10. Damyanova S, Pawelec B, Arishtirova K, Huerta MVM, Fierro JLG. Study of the surface and redox properties of ceria–zirconia oxides. *Appl Catal A Gen*. 2008;337(1):86-96.

11. Capdevila-Cortada M, Vile G, Teschner D, Perez-Ramirez J, Lopez N. Reactivity descriptors for ceria in catalysis. *Appl Catal Environ*. 2016;197:299-312.

12. Puigdollers AR, Schlexer P, Tosoni S, Pacchioni G. Increasing oxide reducibility: the role of metal/oxide interfaces in the formation of oxygen vacancies. *ACS Catal*. 2017;7(10):6493-6513.

13. Miceli P, Bensaid S, Russo N, Fino D. Effect of the morphological and surface properties of CeO_2-based catalysts on the soot oxidation activity. *Chem Eng J*. 2015;278:190-198.

14. Guillén-Hurtado N, Bueno-López A, García-García A. Surface and structural characterisation of coprecipitated $Ce_xZr_{1-x}O_2$ ($0 \le x \le 1$) mixed oxides. *J Mater Sci*. 2012;47(7):3204-3213.

15. Zhang Z, Han D, Wei S, Zhang Y. Determination of active site densities and mechanisms for soot combustion with O_2 on Fe-doped CeO_2 mixed oxides. *J Catal*. 2010;276(1):16-23.

16. Getsoian AB, Zhai Z, Bell AT. Band-gap energy as a descriptor of of catalytic activity for propene oxidation over mixed metal oxide catalysts. *J Am Chem Soc*. 2014;136(39):13684-13697.

17. Mukherjee D, Rao BG, Reddy BM. CO and soot oxidation activity of doped ceria: influence of dopants. *Appl Catal Environ*. 2016;197:105-115.

18. Anantharaman AP, Dasari HP, Lee J-H, Dasari H, Babu GUB. Soot oxidation activity of redox and non-redox metal oxides synthesised by EDTA–citrate method. *Catal Lett*. 2017;147(12):3004-3016.

19. Shannon RD. Revised effective ionic radii and systematic studies of interatomic distances in halides and chalcogenides. *Acta Crystallogr Sect A*. 1976;32(5):751-767.

20. Prasad DH, Park SY, Oh EO, et al. Synthesis of nano-crystalline $La_{1-x}Sr_xCoO_{3-\delta}$ perovskite oxides by EDTA–citrate complexing process and its catalytic activity for soot oxidation. *Appl Catal A Gen*. 2012;447-448:100-106.

21. Tauc J, Grigorovici R, Vancu A. Optical properties and electronic structure of amorphous germanium. *Phys Status Solidi*. 1966;15(2):627-637.

22. Piumetti M, Bensaid S, Russo N, Fino D. Nanostructured ceria-based catalysts for soot combustion: investigations on the surface sensitivity. *Appl Catal Environ*. 2015;165:742-751.

23. Katta L, Sudarsanam P, Thrimurthulu G, Reddy BM. Doped nanosized ceria solid solutions for low temperature soot oxidation: zirconium versus lanthanum promoters. *Appl Catal Environ*. 2010;101(1-2):101-108.

24. Zhu B, Tahara Y, Yasunaga K, Matsui T, Hori F, Iwase A. Study on analysis of crystal structure in CeO_2 doped with Er_2O_3 or Gd_2O_3. *J Rare Earths*. 2010;28(SUPPL. 1):164-167.

25. Reddy BM, Bharali P, Saikia P, et al. Structural characterization and catalytic activity of nanosized $Ce_xM_{1-x}O_2$ (M = Zr and Hf) mixed oxides. *J Phys Chem C*. 2008;112(31):11729-11737.

26. Aneggi E, Wiater D, de Leitenburg C, Llorca J, Trovarelli A. Shape-dependent activity of ceria in soot combustion. *ACS Catal*. 2014;4(1):172-181.

27. Shen Q, Wu M, Wang H, et al. Facile synthesis of catalytically active CeO_2 for soot combustion. *Cat Sci Technol*. 2015;5(3):1941-1952.

28. Thrimurthulu G, Rao KN, Devaiah D, Reddy BM. Nanocrystalline ceria–praseodymia and ceria–zirconia solid solutions for soot oxidation. *Res Chem Intermed*. 2012;38(8):1847-1855.

29. Guillén-Hurtado N, Bueno-López A, García-García A. Catalytic performances of ceria and ceria-zirconia materials for the combustion of diesel soot under NOx/O_2 and O_2. Importance of the cerium precursor salt. *Appl Catal A Gen*. 2012;437-438(2):166-172.

30. Filtschew A, Hofmann K, Hess C. Ceria and its defect structure: new insights from a combined spectroscopic approach. *J Phys Chem C*. 2016;120(12):6694-6703.

31. Mukherjee D, Rao BG, Reddy BM. Characterization of ceria-based nano-oxide catalysts by raman spectroscopy. *Top Catal*. 2017;60(19-20):1673-1681.

32. Vinodkumar T, Durgasr Naga D, Reddy BM. Design of transition and rare earth metal doped ceria nanocomposite oxides for CO oxidation. *Int J Adv Eng Sci*. 2013;5(4):224-231.

33. Lin F, Delmelle R, Vinodkumar T, Reddy BM, Wokaun A, Alxneit I. Correlation between the structural characteristics, oxygen storage capacities and catalytic activities of dual-phase Zn-modified ceria nanocrystals. *Cat Sci Technol*. 2015;5(7):3556-3567.

34. Sudarsanam P, Kuntaiah K, Reddy BM. Promising ceria–samaria-based nano-oxides for low temperature soot oxidation: a combined study of structure–activity properties. *New J Chem*. 2014;38(12):5991-6001.

35. Guo M, Lu J, Wu Y, Wang Y, Luo M. UV and visible Raman studies of oxygen vacancies in rare-earth-doped ceria. *Langmuir*. 2011;27(7):3872-3877.

36. Lin X, Li S, He H, et al. Evolution of oxygen vacancies in MnO_x-CeO_2 mixed oxides for soot oxidation. *Appl Catal Environ*. 2018;223:91-102.

37. Zhang W, Niu X, Chen L, Yuan F, Zhu Y. Soot combustion over nanostructured ceria with different morphologies. *Sci Rep*. 2016;6:1-10.

38. Ansari SA, Khan MM, Ansari MO, Kalathil S, Lee J, Cho MH. Band gap engineering of CeO_2 nanostructure using an electrochemically active biofilm for visible light applications. *RSC Adv*. 2014;4(32):16782-16791.

39. Mia MNH, Pervez MF, Hossain MK, et al. Influence of Mg content on tailoring optical bandgap of Mg-doped ZnO thin film prepared by sol-gel method. *Results Phys*. 2017;7:2683-2691.

40. Andana T, Piumetti M, Bensaid S, Russo N, Fino D. Nanostructured ceria-praseodymia catalysts for diesel soot combustion. *Appl Catal Environ*. 2016;197:125-137.

41. Devaiah D, Tsuzuki T, Boningari T, Smirniotis PG, Reddy BM. $Ce_{0.80}M_{0.12}Sn_{0.08}O_{2-\delta}$ (M = Hf, Zr, Pr, and La) ternary oxide solid solutions with superior properties for CO oxidation. *RSC Adv*. 2015;5(38):30275-30285.

42. Fang P, Luo M-F, Lu J-Q, Cen S-Q, Yan X-Y, Wang X-X. Studies on the oxidation properties of nanopowder CeO_2-based solid solution catalysts for model soot combustion. *Thermochim Acta*. 2008;478(1-2):45-50.

43. Anantharaman AP, Geethu J, Mohammed Rishab P, et al. Ceria-samarium binary metal oxides: a comparative approach towards structural properties and soot oxidation activity. *Mol Catal*. 2018;451:247-254.

44. Anantharaman AP, Dasari HP, Dasari H, Babu GUB. Surface morphology and phase stability effect of ceria-hafnia (CH_x) binary metal oxides on soot oxidation activity. *Appl Catal A Gen*. 2018;566:181-189.

SUPPORTING INFORMATION

Additional supporting information may be found online in the Supporting Information section at the end of the article.